Synthesis of Colloidal MnAsxSb1-x Nanoparticles: Compositional Inhomogeneity and Magnetic Consequences

Journal:	*Journal of Materials Chemistry C*
Manuscript ID	TC-ART-05-2021-002479.R1
Article Type:	Paper
Date Submitted by the Author:	04-Aug-2021
Complete List of Authors:	Hettiarachchi, Malsha; Wayne State University, Department of Chemistry Su'a, Tepora; Wayne State University, Department of Chemistry Abdelhamid, Ehab; Wayne State University, Pokhrel, Shiva; Wayne State University, Physics and Astronomy Nadgorny, Boris; Wayne State University, Physics & Astronomy Brock, Stephanie; Wayne State University, Department of Chemistry

SCHOLARONE™
Manuscripts

Synthesis of Colloidal MnAs$_x$Sb$_{1-x}$ Nanoparticles: Compositional Inhomogeneity and Magnetic Consequences

Malsha A. Hettiarachchi,[1] Tepora Su'a,[1] Ehab Abdelhamid,[2] Shiva Pokhrel,[2] Boris Nadgorny,[2]

Stephanie L. Brock[1]

[1]Department of Chemistry, Wayne State University, Detroit, MI, 48202 USA

[2]Department of Physics and Astronomy, Wayne State University, Detroit, MI 48201, USA

Abstract

The ternary manganese pnictide phases, MnAs$_{1-x}$Sb$_x$, are of interest for magnetic refrigeration and waste heat recovery due to their magnetocaloric properties, maximized at the Curie temperature (T_C), which varies from 580-240 K, depending on composition. Nanoparticles potentially enable application in microelectronics (cooling) or graded composites that can operate over a wide temperature range, but manganese pnictides are synthetically challenging to realize as discrete nanoparticles and their fundamental magnetic properties have not been extensively studied. Accordingly, colloidal synthesis methods were employed to target discrete MnAs$_x$Sb$_{1-x}$ nanoparticles (x = 0.1 - 0.9) by arrested precipitation reactions of Mn$_2$(CO)$_{10}$ with (C$_6$H$_5$)$_3$As=O and (C$_6$H$_5$)$_3$Sb in coordinating solvents. The MnAs$_x$Sb$_{1-x}$ particles are spherical in morphology with average diameters 10 – 13 nm (standard deviations < 20% based on transmission electron microscopy analysis). X-ray fluorescence spectroscopy measurements on ensembles showed that all phases had an excess of Sb relative to the targeted composition, whereas energy dispersive spectroscopic mapping data of single particles revealed that the nanoparticles are inhomogeneous, adopting a core-shell structure, with the amorphous shell rich in Mn and O (and sometimes Sb) while the crystalline core is rich in Mn, As, and Sb. Magnetization measurements of the

nanoparticle ensemble demonstrated the presence of both ferromagnetic and paramagnetic phases. By combining the magnetization measurements with precision chemical mapping and simple modeling, we were able to unambiguously attribute ferromagnetism to the $MnAs_xSb_{1-x}$ crystalline core, whereas paramagnetism was attributed to the amorphous shell. Magnetization measurements at variable temperatures were used to determine the superparamagnetic transition of the nanoparticles, although for some compositions and particle sizes the blocking temperature exceeded room temperature. Preliminary magnetic studies also revealed a conventional dependence between core size and coercivity, in spite of variable compositions of the nanoparticles, an unexpected result.

Introduction

Transition metal pnictides (pnictide = Pn = Group 15 element anion) exhibit a wide range of properties that depend sensitively on their composition, structure and particle size.[1-4] Among these, the equimolar manganese pnictides (MnPn) are of particular interest because of their potential application in spintronics,[5-8] solid-state magnetic refrigeration and waste heat recovery due to their sizeable ferromagnetic and magnetocaloric properties.[9-12] For example, epitaxial MnSb-GaAs heterostructures function as spin light-emitting-diodes due to magnetic polarization of excited spins in GaAs by MnSb,[7] whereas strained MnAs nanoparticles on InAs nanowires function as single magnetic bits.[5] With respect to room-temperature magnetic refrigeration applications MnAs is of interest due to the large magnetic entropy change associated with the magnetostructural transition from hexagonal (NiAs-type, α-MnAs) to orthorhombic (MnP-type, β-MnAs) at the ferromagnetic transition temperature (T_C =313-318K).[13-19] The temperature at which this effect is

maximized can be chemically tuned by substitution of As for P (up to 4 %) enabling suppression by as much as 30 K,[20-24] thus potentially widening the temperature range for operation in a compositionally modulated composite.[25-30]

Nanostructuring of magnetocalorics enables temperature control in small devices such as microfluidic synthesizers and microelectronics, but has also been embraced because it enables processability and composite formation (whereby a broad operation temperature can be obtained by mixing phases with different T_C's [25-30]) and is purported to lead to reduction of thermal and magnetic hysteresis.[12] Nanostructures also offer the opportunity of potentially realizing metastable structures that can work harmoniously to exploit giant magnetocaloric materials—even when there are considerable hysteretic effects that would normally compromise efficiency.[31, 32]

In an effort to better understand how nanostructuring impacts the magnetic properties of MnPn relevant to applications in magnetic refrigeration, we have developed synthetic methods that enable formation of discrete nanoparticles of MnAs, $MnAs_{1-x}P_x$, $(x \leq 0.1)$ and MnSb with relatively low polydispersity and have evaluated their fundamental magnetic properties.[33-37] Among the notable and unexpected properties include a significant suppression of the thermal hysteresis in MnAs and a dramatic decrease in the magnetostructural phase transition temperature along with large co-existence regions induced upon P incorporation, distinct to what is reported for comparable bulk materials.[34, 36]

In the present contribution, our target for colloidal synthesis is another well-known magneto-caloric ternary material that enables compositional tuning over a much wider temperature range, $MnAs_xSb_{1-x}$ $(x = 0.1-0.9)$.[38-46] The MnSb (NiAs-type) end-product is characterized by a magnetic transition at $T_C = 580$ K that drops monotonically to 240 K upon substitution of up to 70% of the Sb by As. However, from $x = 0.7$ to 0.85, the T_C increases from 240-280 K, and for x

> 0.85 the T_C increases further to 315 K, and is accompanied by a structural change from NiAs-type to MnP-type ($\alpha\rightarrow\beta$) characteristic of MnAs. Our goal is to realize discrete nanoparticles of $MnAs_xSb_{1-x}$ at targeted values of x that span the solid-solution and evaluate how the fundamental magnetic properties of the particles (T_C, thermal and magnetic hysteresis, blocking temperature and coercivity) compare to the established bulk-phase properties.

Here we report the first synthesis of colloidal $MnAs_xSb_{1-x}$ (x = 0.1-0.9) nanoparticles. In contrast to our expectation and the behavior of bulk-phases, where the solid-solution is single phase across all x, we find that phase segregation is endemic, leading to compositional heterogeneity. In colloidal synthesis, such phase-segregation is known to represent a significant challenge when more complex formulations, e.g., ternary or quaternary compositions, are targeted, requiring considerable optimization.[47, 48] On the other hand, nanoscale heterogeneities can be critical components in materials that display interesting magnetic[49-51] and catalytic properties.[52, 53] In the present case, and quite unexpectedly, we find that the nanoscale magnetic behavior—in spite of the significant compositional variation arising both from changes in x and localized phase-segregation of the pnictide—exhibits a well-established size-dependent trend in coercivity at low temperature ($T << T_C$). These data suggest that the change in the nanoparticle composition does not systematically affect magnetic anisotropy of the nanoparticles in this system.

Methods

Materials

Manganese carbonyl [$Mn_2(CO)_{10}$ (98%)], triphenyl antimony [Ph_3Sb (99%)], triphenylarsine oxide [Ph_3AsO (97%)], 1-octadecene (1-ODE) (90%, technical grade) and trioctylphosphine oxide

[TOPO (90%, technical grade)] were purchased from Sigma Aldrich, Inc. Chloroform was purchased from Fisher Scientific, and ethanol (200 proof) was purchased from Decon laboratories. TOPO was purified by the fractional distillation method.[54] All other chemicals were used as received.

Synthesis of MnAs$_x$Sb$_{1-x}$ Nanoparticles: slow heating, one-pot synthesis

$Mn_2(CO)_{10}$ (0.5-1.2 mmol), Ph_3Sb (0.1-0.9 mmol) and Ph_3AsO (0.1-0.9 mmol) were mixed along with 1-ODE (20-30 mL) and TOPO (4.0 g) in a single Schlenk flask in a glove box filled with argon. The sealed Schlenk flask was then removed from the glove box to a Schlenk line in a fume hood. The contents in the flask were evacuated for 20 min followed by Ar purging for about another 20 min at 60 °C. The contents were then heated slowly (20 °C/10 min), to avoid any volatilization of $Mn_2(CO)_{10}$, up to 180 °C under Ar. Then, the temperature was rapidly increased up to 250-300 °C and maintained for 1-6 h. The final black product was allowed to cool naturally to room temperature. The product was dispersed in chloroform and precipitated with ethanol, followed by centrifugation. This process of dispersion/precipitation was repeated several times and then the product was dried under vacuum.

Characterization

Powder X-Ray Diffraction

Room temperature Powder X-Ray Diffraction (PXRD) patterns were acquired in the range $2\Theta =$ 20–70° on a Bruker Phaser II model X-ray diffractometer equipped with a Cu anode. Samples were placed on a zero-background quartz holder for measurements.

Transmission Electron Microscopy

Transmission Electron Microscopy (TEM) images were obtained on a JEOL 2010 transmission electron microscope operated at 200 kV. The specimens were prepared by dispersing the solid sample with sonication in chloroform and supporting the particles on a 200 mesh Cu grid coated with a carbon film.

High Angle Annular Dark Field- Scanning Transmission Electron Microscopy, Energy Dispersive Spectroscopy, and Elemental Mapping

The elemental composition of individual nanoparticles was analyzed using an FEI, Talos F200X High Angle Annular Dark Field- Scanning Transmission Electron Microscope (HAADF-STEM) equipped with XFEG and Super-X EDS technology, operated at 200 kV.

X-Ray Fluorescence Spectrometry

The elemental compositions of Mn, As, and Sb were analyzed with a SHIMADZU EDX-7000 energy dispersive X-Ray Fluorescence Spectrometer (XRF), using PCEDX-Navi software, operating in air with the collimator size of 10 mm. Solid samples were placed in the middle of a Mylar® cup, which was then placed on the beam window located on the sample plate. The X-ray generator had Rhodium target operating at 50 kV (Rh 50) with a 26 µA current, and the detector was a silicon drift detector.

Magnetic Measurements

Magnetic measurements were acquired on solid $MnAs_xSb_{1-x}$ nanoparticle powders (previously stored under an inert atmosphere) in a silica gel capsule. A Quantum Design PPMS 6000 system was used to record the temperature-dependent DC magnetization data, Zero-Field Cooling (ZFC) and Field Cooling (FC), under 100 Oe DC field, between 10 K and 320 K. M vs H data was also

collected on a Quantum Design PPMS 6000 system at 50 K and 300 K, sweeping fields from +10,000 Oe to -10,000 Oe. All data are normalized to moles of Mn in the sample, determined by ICP-MS.

Inductively Coupled Plasma – Mass Spectrometry

Moles of Mn in the sample were obtained using an Agilent 7700x Series Inductively Coupled Plasma – Mass Spectrometer (ICP-MS). Solid powders of $MnAs_xSb_{1-x}$ nanoparticles (~1 mg) were completely dissolved in concentrated nitric acid (2 mL) and then diluted to 100 mL in a volumetric flask with 2% HNO_3 acid. This was further diluted by taking a 0.10 mL aliquot and diluting to 100 mL using 2% HNO_3 acid. 2% HNO_3 acid served as the blank solution. In order to calibrate the instrument, Mn standard solutions (300, 500, 700, 1200, 1500, 1800, 2500 ppb) were prepared by serial dilution of Mn stock solutions.

Results and Discussion

Colloidal synthesis of $MnAs_xSb_{1-x}$ nanoparticles.

We expected to be able to form nanocrystal solid solutions across all x for $MnAs_xSb_{1-x}$ based on (1) the established existence of solid solutions in bulk phase syntheses[38, 41-44] and (2) the similarity of reaction conditions needed to obtain the end-products, MnSb (250-280 ºC, Ph_3Sb)[35] and MnAs (275-330 ºC, $Ph_3As=O$).[34] The reactions have a common solvent system (octylether plus trioctylphosphine oxide as a stabilizing ligand), but MnSb reactions typically produce Sb byproducts unless the Mn is present in large excess (80% by mole, 280 ºC)[35] or an external reductant ($NaBH_4$, 250 ºC)[37] is employed. This we attribute to slow reactivity between Mn and Sb

precursors leading to competitive formation of MnO_b phases due to reaction with adventitious oxygen unless $NaBH_4$ is present as an oxygen getter.[37] This contrasts with the synthesis of antimonides of less electropositive metals, where oxidation is less prominent.[55, 56] With respect to MnAs, reactions conducted with 10% excess Mn using high-temperature injection (330 ºC) resulted in incorporation of P (up to ca 4%) from reaction with TOPO stabilizing ligands, whereas slow-heating to 275 ºC produced undoped MnAs.[36] Based on these data, we elected to start our exploration of phase space at the low-temperature end (250 ºC) with a slight excess of Mn (10%), targeting the 1:1 product ($MnAs_{0.5}Sb_{0.5}$).

Fig. S1, ESI† shows the PXRD pattern obtained for the product from the reaction of 0.5 mmol $Ph_3As=O$, 0.5 mmol Ph_3Sb, and 0.55 mmol $Mn_2(CO)_{10}$ carried out at 250°C for 3 h. The PXRD pattern is consistent with formation of an MnSb-type phase (hexagonal, NiAs-type) with a significant shift to higher 2Θ values, consistent with incorporation of the smaller radius As. These peaks are broad, indicative of nanocrystal formation, but also asymmetric, raising the possibility of multiple $MnAs_{1-x}Sb_x$ phases co-existing (polydispersity in composition). At the same time, large quantities of crystalline Sb are evident, manifesting as sharp peaks, consistent with bulk-phase precipitation. As shown in **Fig. S2, ESI**†, decreasing the reaction time from 3 to 1 h reduced, but did not eliminate, Sb precipitation, and exacerbated the peak asymmetry (suggesting yet more polydispersity in composition); whereas increasing the time to 6 h produced more symmetric peaks (less polydispersity) but led to enhanced Sb precipitation. Increasing temperature beyond 250 ºC also resulted in more Sb byproduct formation and greater peak asymmetry (**Fig. S3, ESI**†).

Based on our previous experience with MnSb, we explored two approaches to eliminate Sb precipitation: (1) increase Mn concentration or (2) add $NaBH_4$. According to **Fig. 1**, the elemental Sb peak appears at *ca.* 28 degrees (2Θ) when the Mn amount is 1.1 mmol (vs. 1 mmol

Sb), diminishes when the Mn amount is 1.2 mmol, and disappears when the Mn amount is 1.5 mmol. Moreover, in the cases of 1.1 and 1.2 mmol of Mn addition, the peaks for the $MnAs_xSb_{1-x}$ phase have a notable shoulder at high 2Θ of intensity approaching that of the main peak. However, when sufficient Mn is present, consuming all Sb, the shoulder is diminished in intensity. Collectively taken, the excess Mn is likely reacting with elemental Sb in the reaction mixture. The necessity of excess $Mn_2(CO)_{10}$ in the reaction mixture could be due to the high volatility of $Mn_2(CO)_{10}$ and/or '*in-situ*' oxidation by an adventitious oxygen source.[35, 37] Unfortunately, $NaBH_4$ addition leads to phase segregation with PXRD reflections indicative of formation of MnSb, MnAs, and elemental Sb. (**Fig. S4, ESI†**). Accordingly, this approach was not pursued further.
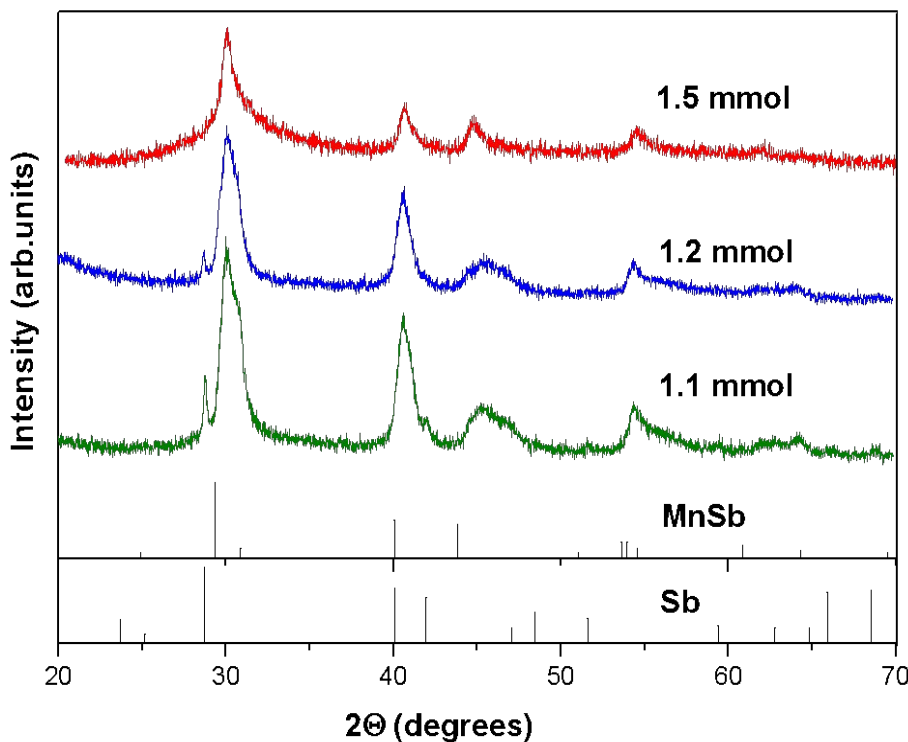
Fig. 1: PXRD patterns of MnAs$_{0.5}$Sb$_{0.5}$ (target composition) synthesized using different amounts of Mn (MnSb-PDF#-03-065-0388, Sb-PDF#-00-035-0732)

Structure, morphology, composition, and elemental mapping of MnAs$_{1-x}$Sb$_x$ nanoparticles.

After optimizing the reaction conditions for the 50:50 composition, a series of compositions were synthesized targeting x = 0.1 to 0.9. The PXRD and TEM images of nanoparticles of MnAs$_x$Sb$_{1-x}$ (x = 0.1 - 0.8) are shown in **Fig. 2** and **3,** respectively, and the data for x = 0.9 is shown in **Fig. 4.**

The PXRD patterns were normalized with respect to an internal Si standard (Si peaks are indicated as asterisks marks near 28° and 47° 2Θ), **Fig. 2**. PXRD patterns of materials with composition x = 0.1 - 0.8 were indicative of the NiAs-type, characteristic of MnAs and MnSb end members and MnAs$_x$Sb$_{1-x}$ for x < 0.85. Relative to MnSb (PDF#: 03-065-0388) there is a notable

shift to higher 2Θ values with increasing As introduction, indicative of lattice compression upon substitution of Sb with the smaller pnicogen, consistent with what would be expected upon formation of a solid-solution. Additionally, there are compositional variations in the peak breadths indicative of changes in crystallite size. These changes in lattice parameters and crystallite sizes are discussed more fully below. As shown in **Fig. 3**, these nanoparticle samples have low polydispersity and the particles are spherical with an average diameter of *ca*. 10-13 nm.
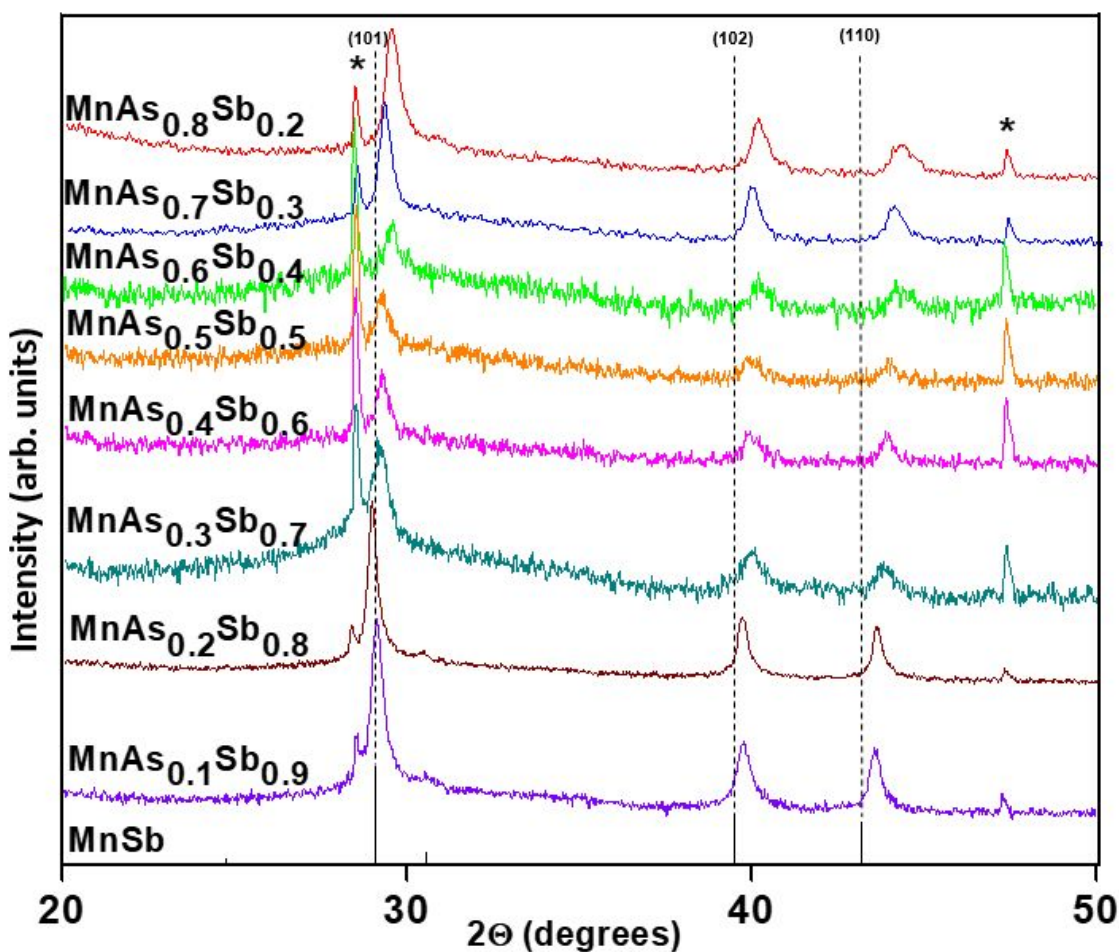

Fig. 2: PXRD pattern of $MnAs_xSb_{1-x}$ (x = 0.1 - 0.8) nanoparticles normalized with respect to Si standard. Peaks for Si are shown with asterisks (MnSb-PDF#-03-065-0388)

As anticipated, the PXRD pattern of the target composition $MnAs_{0.9}Sb_{0.1}$ was closely related to the orthorhombic β-MnAs phase (**Fig. 4 (a)**), expected to form for 0.85 < x < 1.0 and the nanoparticles appear spherical with the average diameter of *ca*.13 nm (**Fig. 4 (b)**).
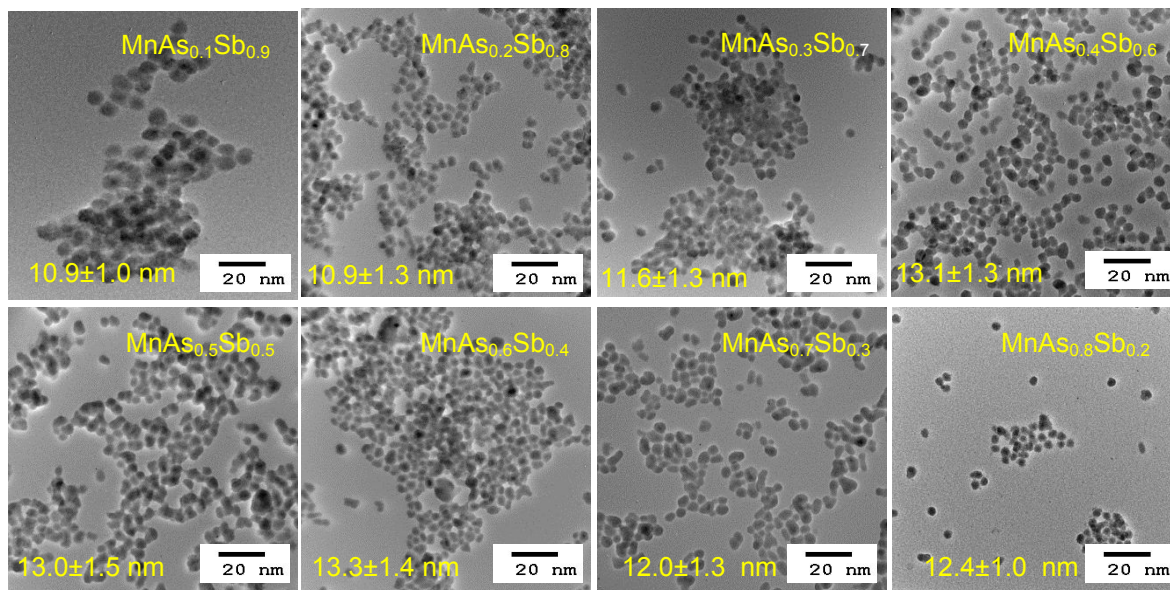
Fig. 3: Representative TEM images of the $MnAs_xSb_{1-x}$ (x = 0.1 - 0.8) nanoparticles (target compositions indicated).
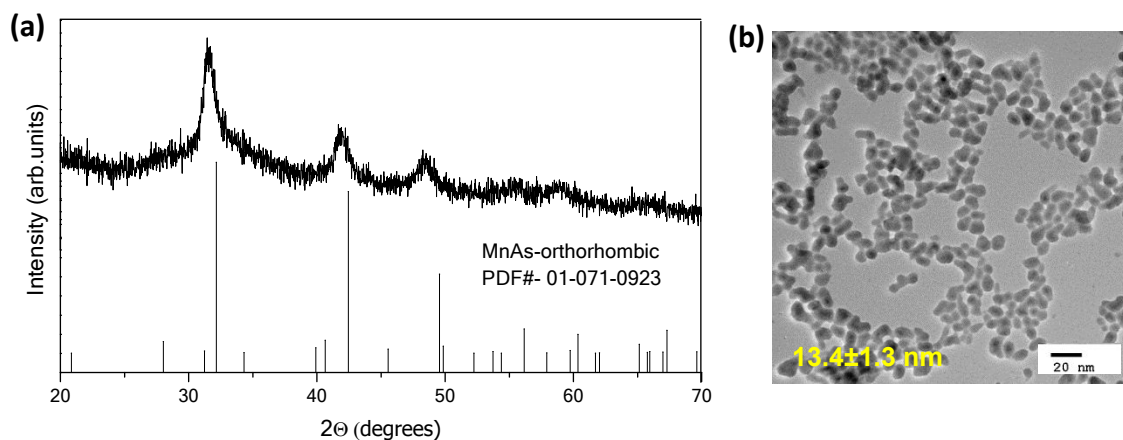
Fig. 4: (a) PXRD pattern **(b)** TEM image of target composition $MnAs_{0.9}As_{0.1}$ nanoparticles.

Lattice Refinement and Composition Analysis

The cell parameters of the compounds with targeted ratios from $MnAs_{0.1}Sb_{0.9}$ to $MnAs_{0.8}Sb_{0.2}$ were refined by CELREF version 3, using the three high-intensity peaks in the PXRD [(011), (012), and (110), indexed based on MnSb], calibrated against Si as an internal standard. The refined lattice parameters a, c, and the cell volume of the hexagonal crystal structures are

12

given in **Table 1**. The graphical representations are shown in **Fig. 5**. The parent structures, MnAs and MnSb, have a difference in the *a* axis of 13%, while the variation of the *c* axis is around 1%.[57] The data reinforce the suggestion of solid-solution formation as indicated by relative peak shifts in the PXRD; the *a* and V parameters decreasing roughly linearly as the As substitutes for Sb in the hexagonal structure where *c* is largely unchanged.

Table 1: Refined lattice parameters of hexagonal crystal structures of $MnAs_{0.1}Sb_{0.9}$ to $MnAs_{0.8}Sb_{0.2}$ (target compositions)

Target composition	*a* [Å]	*c* [Å]	*V* [Å³]
$MnAs_{0.1}Sb_{0.9}$	4.1300(62)	5.7897(56)	85.52(15)
$MnAs_{0.2}Sb_{0.8}$	4.1228(36)	5.8048(33)	85.45(09)
$MnAs_{0.3}Sb_{0.7}$	4.1073(41)	5.7829(38)	84.49(10)
$MnAs_{0.4}Sb_{0.6}$	4.1095(32)	5.7860(30)	84.62(08)
$MnAs_{0.5}Sb_{0.5}$	4.1049(10)	5.7886(09)	84.47(03)
$MnAs_{0.6}Sb_{0.4}$	4.0919(17)	5.7825(15)	83.85(04)
$MnAs_{0.7}Sb_{0.3}$	4.0874(02)	5.8008(02)	83.93(01)
$MnAs_{0.8}Sb_{0.2}$	4.0898(51)	5.7891(48)	83.86(13)

However, the chemical analysis data tells a different story. As a means of probing the bulk (average) composition, solid powder samples of the targeted compositions were probed by X-ray fluorescence (XRF). As shown in **Table 2** while
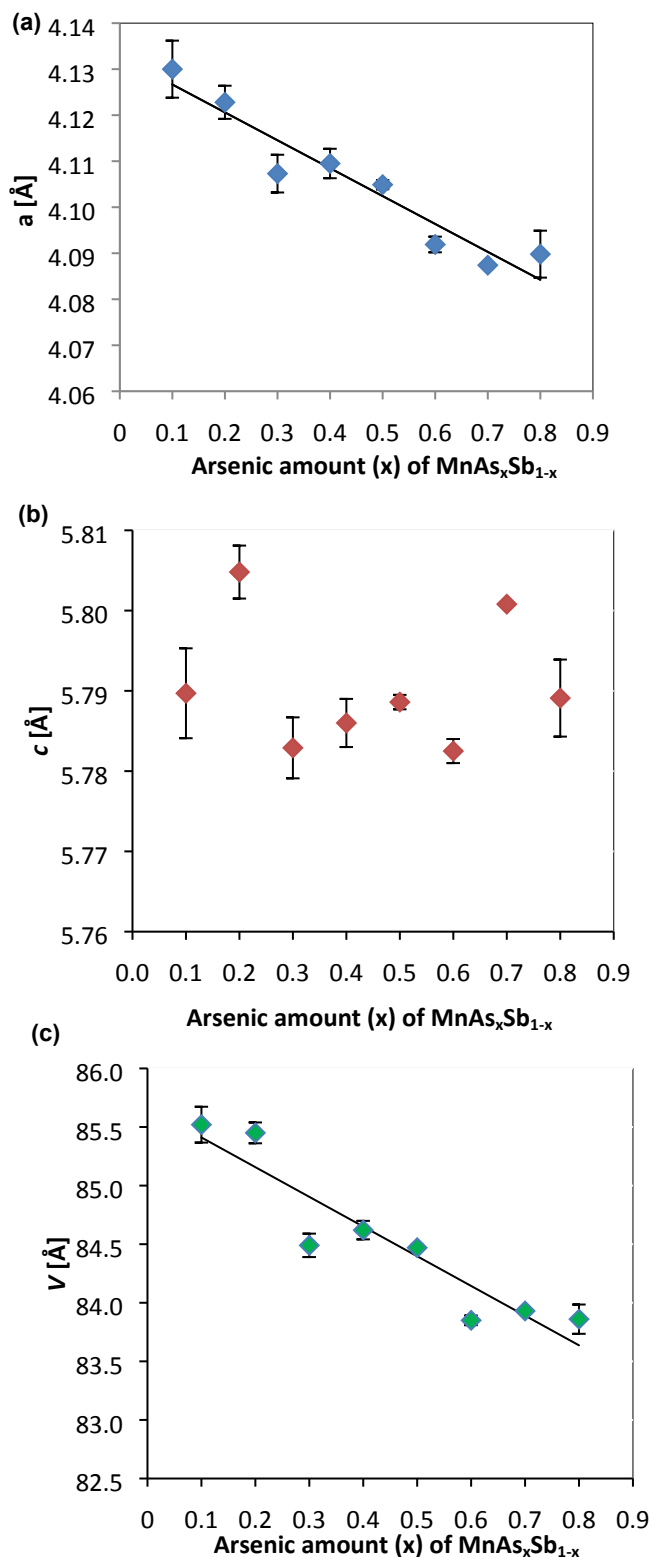

Fig. 5: The refined lattice parameters of target compositions $MnAs_xSb_{1-x}$ (x = 0.1 - 0.8) **(a)** *a* axis **(b)** *c* axis **(c)** cell volume, V.

we do see a natural increment in As incorporation as the As/Sb ratio is increased in the synthesis, the As incorporation falls far short of the targeted composition. The relative differences, most notable at intermediate compositions, are shown in **Fig. 6**, where the observed concentration x' vs. targeted x is plotted alongside the ideal relationship (indicated by a solid red line).

Table 2: Differences between the target and the actual compositions of $MnAs_xSb_{1-x}$ nanoparticles determined by XRF.

| Target composition	Actual composition
$MnAs_{0.10}Sb_{0.90}$	$MnAs_{0.03}Sb_{0.95}$
$MnAs_{0.20}Sb_{0.80}$	$MnAs_{0.08}Sb_{0.92}$
$MnAs_{0.30}Sb_{0.70}$	$MnAs_{0.13}Sb_{0.87}$
$MnAs_{0.40}Sb_{0.60}$	$MnAs_{0.14}Sb_{0.86}$
$MnAs_{0.50}Sb_{0.50}$	$MnAs_{0.31}Sb_{0.69}$
$MnAs_{0.60}Sb_{0.40}$	$MnAs_{0.40}Sb_{0.60}$
$MnAs_{0.70}Sb_{0.30}$	$MnAs_{0.52}Sb_{0.48}$
$MnAs_{0.80}Sb_{0.20}$	$MnAs_{0.57}Sb_{0.43}$
$MnAs_{0.90}Sb_{0.10}$	$MnAs_{0.85}Sb_{0.15}$
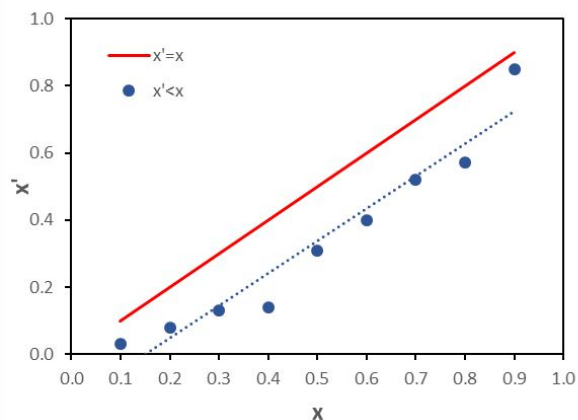
Fig. 6: Graphical representation of ideal composition vs actual composition (the dashed line provides a guide to the eye)

According to **Table 2**, the actual compositions deviate from the target compositions by having a significantly lower As content relative to Sb, suggesting As incorporation is inhibited, likely due to the lower reaction temperature employed that is less ideal for the As end-product, MnAs. Indeed, in reviewing the lattice parameters in **Fig. 5**, and assuming solid-solution formation between MnAs (a = 3.72 Å, c = 5.71 Å , V = 67.6 Å³) and MnSb (a =4.14Å, c = 5.84Å, V = 86.7Å³) follows Vegard's Law, the data suggest the maximum incorporation of As into unstrained crystalline MnSb (NiAs-type) is no more than 20%, even lower than what is indicated by the actual stoichiometry. Note that the incorporation of As increases when targeting the one composition adopting the MnP-type (β-MnAs) structure ($MnAs_{0.90}Sb_{0.10}$ targeted = $MnAs_{0.85}Sb_{0.15}$ observed).

To better understand how this dearth of As in NiAs-type $MnAs_xSb_{1-x}$ impacts the particle homogeneity, HAADF-STEM and elemental distribution mapping within individual nanoparticles was conducted for representative nanoparticles with actual composition $MnAs_{0.31}Sb_{0.69}$ (target composition: $MnAs_{0.5}Sb_{0.5}$). As shown by HAADF-STEM data in **Fig. 7a**, individual nanoparticles within these samples are heterogeneous in nature. $MnAs_{0.31}Sb_{0.69}$ is composed of a high contrast core and a lower contrast shell. Amorphous oxide shells are quite common for MnSb or MnAs[34-37] with the combination of high surface area and the highly reduced nature of the target phases contributing to rapid surface oxidation upon exposure to ambient conditions. Prior mapping data on MnSb and MnAs shows the amorphous shells typically have the same metal: pnictogen ratio as the crystalline cores, again contributing to the notion that the amorphous shell is a consequence of surface oxidation of manganese pnictide, not, for example, deposition of MnO_b on the manganese pnictide particle surface.[34-37]
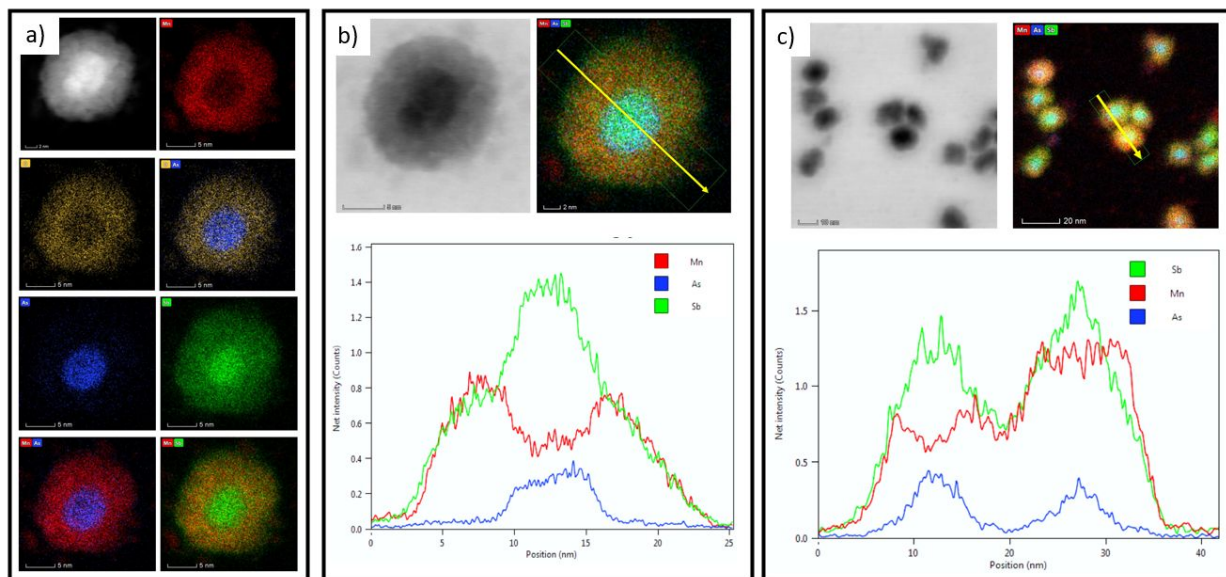
Fig. 7: (a): HAADF-STEM of ca 13 nm diameter $MnAs_{0.31}Sb_{0.69}$ nanoparticle and elemental mapping analysis of Sb (green), Mn (red), As (blue), O (yellow) and overlapping panels of (O+Sb), (Mn+As), and (Mn+Sb). **(b)**: Line scan elemental analysis of a single $MnAs_{0.31}Sb_{0.69}$ nanoparticle along the yellow line. **(c)**: Line scan elemental analysis of multiple $MnAs_{0.31}Sb_{0.69}$ nanoparticles along the yellow line.

A different outcome is revealed for $MnAs_{1-x}Sb_x$ particles by elemental mapping, **Fig. 7a**; Mn (in red) is present throughout the entire particle, but more concentrated in the shell area, where O (yellow) also appears exclusively. In contrast, As (in blue) is essentially concentrated in the core. Although, a considerable amount of Sb (green) is present in the core, it is generally distributed throughout the entire particle. From the line scan of a single particle, **Fig. 7b,** the inhomogeneity within the particle becomes more apparent. The shell has a high concentration of Mn and Sb in approximately equimolar amounts, whereas As is largely segregated to the core. Likewise, a line scan of multiple particles, **Fig 7c,** reveals that the Mn, As, and Sb concentration may vary from particle to particle but all elements are detected within each individual particle. Similar trends in elemental distributions are observed in representative compositions adopting the NiAs-type structure at the Sb-rich end (actual composition: $MnAs_{0.12}Sb_{0.88}$, **Fig. 8)** and the As-rich end (actual composition: $MnAs_{0.48}Sb_{0.52}$, **Fig. S5, ESI†**) but in these cases, both the As and Sb are co-localized in the core and absent in the shell, and the shell appears to be composed only of Mn and O. These data underscore the complexity of the mixed-pnicogen system relative to the well-behaved end-members and suggest surface oxide can arise directly from the synthesis (i.e., MnO_b deposition) and not exclusively from exposure of pristine Mn-pnictide surfaces to air. Notably, nano-diffraction confirms the crystallinity of the core (see **Fig. 8**). Considering this data along with the lattice parameters, we propose a model for NiAs-type $MnAs_xSb_{1-x}$ consisting of a crystalline core, $MnAs_{0.2-y}Sb_{0.8+y}$, within an amorphous shell of MnO_b or $MnSbO_b$. Moreover, based on differences in peak breadths noted in the PXRD patterns in **Fig. 2**, we expect that the size of the crystalline core is not uniform from sample-to-sample. This conclusion is supported by the magnetic property investigation as discussed below.
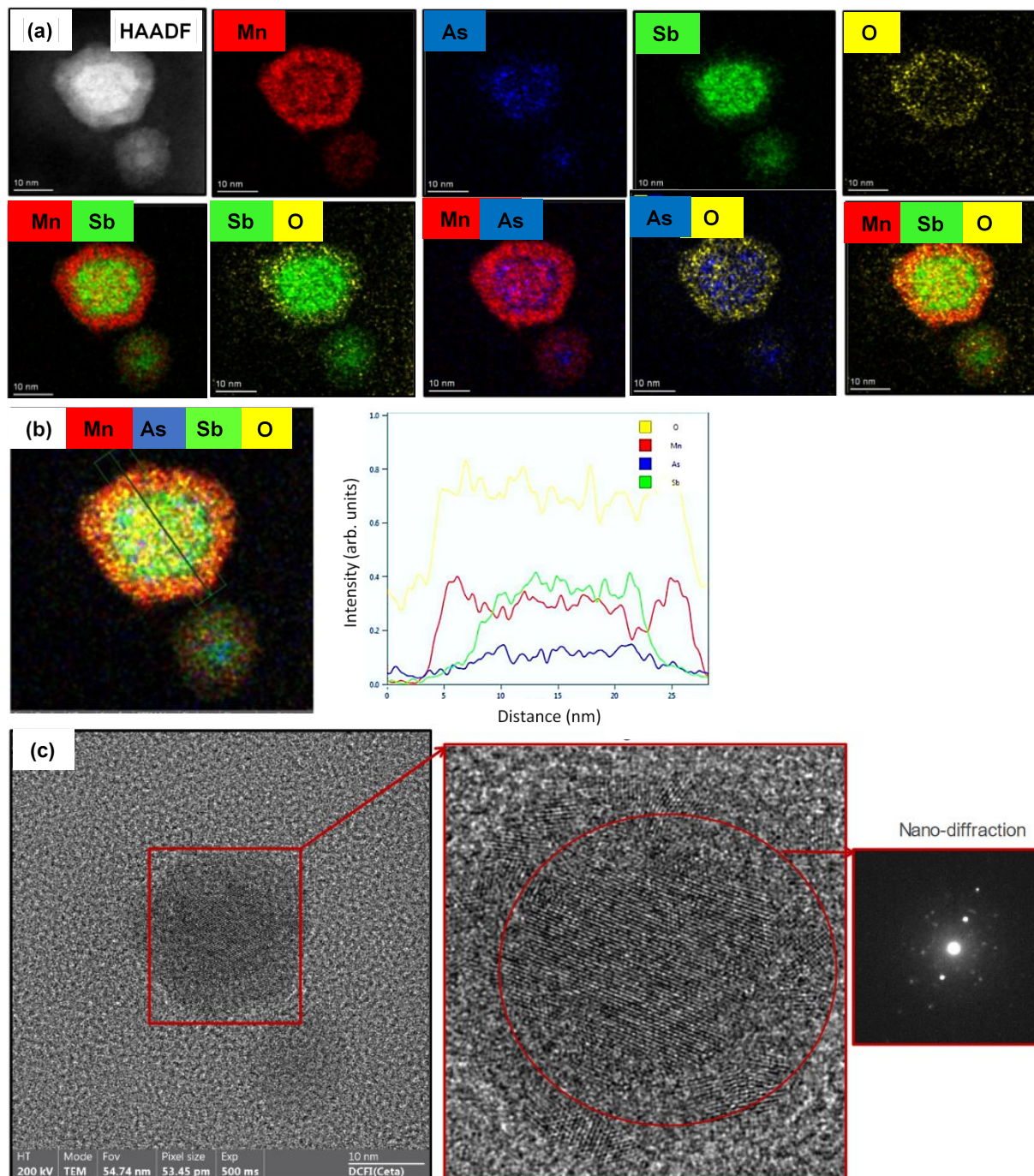
Fig. 8: **(a)** HAADF-STEM of a nanoparticle of observed stoichiometry $MnAs_{0.12}Sb_{0.88}$ (targeted composition $MnAs_{0.30}Sb_{0.70}$) with elemental mapping analysis. **(b)** Line scan elemental analysis along the black line (left) and plot of relative intensity of Mn, As, Sb, O as a function of distance (right). **(c)** HRTEM image depicting the core-shell nature of $MnAs_{0.12}Sb_{0.88}$ nanoparticle showing lattice fringes indicative of core crystallinity, affirmed by the nano-diffraction pattern.

## Magnetic Properties of $MnAs_xSb_{1-x}$ nanoparticles

In order to evaluate the magnetic properties of these compositions with respect to the compositional inhomogeneity and the refined lattice parameters, the temperature (T) dependence of the molar magnetization (M, normalized to Mn moles) was collected under Zero-Field-Cooled (ZFC) and Field-Cooled (FC) conditions in the temperature range 10-320 K under an external magnetic field of 100 Oe; the corresponding magnetic field dependence (H) of the molar magnetization (M) was determined at 50 and 300 K. These data are presented in **Fig. 9** for the targeted composition $MnAs_{0.50}Sb_{0.50}$ nanoparticles (actual composition: $MnAs_{0.31}Sb_{0.69}$) and the data for all other compositions are shown in **Figs. 10, 11**.
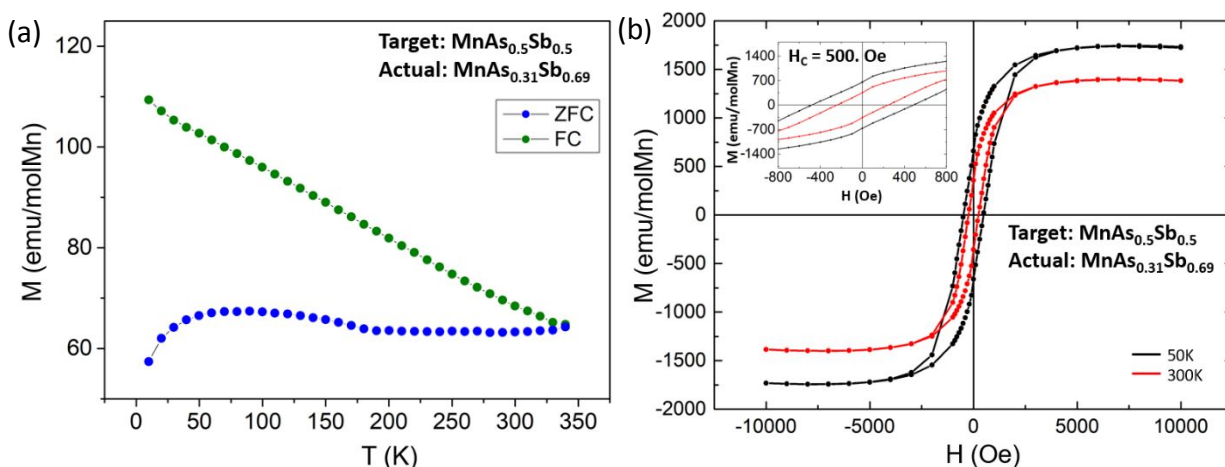
Fig. 9: Magnetic data for $MnAs_{0.31}Sb_{0.69}$ **(a)** Temperature dependence of the DC molar magnetization (M) (normalized to Mn moles) recorded under Zero-Field-Cooled (ZFC) and Field-Cooled (FC) conditions (collected at 100 Oe) **(b)** Field dependence of the DC molar magnetization (M) (normalized to Mn moles) recorded at different magnetic fields (H) at 300 K and 50 K. The inset shows an enlarged image of the loop of the hysteresis curves obtained at 300 K and 50 K.

For well-behaved low-polydispersity superparamagnetic nanoparticles with blocking temperatures (T_B) in the range of study, the expected behavior in the M vs T plot would be a pronounced peak in the ZFC and this would ideally be maximized where the ZFC and FC curves

intersect. Below this temperature, we would expect the particles to behave like a regular ferromagnet, showing a distinct hysteresis in the M vs. H plot reflecting the coercive field required to drive the moment to zero. Above T_B, in the superparamagnetic regime, the timescale of the experiments is sufficiently long to enable thermal relaxation of the ferromagnetic moments, producing M vs H plots that exhibit saturation, but no hysteresis (zero coercivity). However, the transition between ferromagnetism and superparamagnetism depends strongly on the particle size and the anisotropy (magnetic and/or shape) of a nanoparticle, and hexagonal $MnAs_xSb_{1-x}$ is characterized by a large intrinsic magnetocrystalline anisotropy which is expected to enable coercive behavior even among nanometer-size particles, such as those explored here. At the same time, we note that while the polydispersity of the particles used in this study is fairly low (about 10% deviation from the average value), it is large enough to produce a noticeable variation in the blocking temperature, which is proportional to the volume of the nanoparticles. For example, for the $MnAs_{0.50}Sb_{0.50}$ targeted composition the volume varies by approximately a factor of two, thus significantly broadening the transition to the superparamagnetic limit. In such cases, when there is a distribution of blocking temperatures, the intersection of the ZFC and FC plot may not coincide with the maximum in the ZFC.
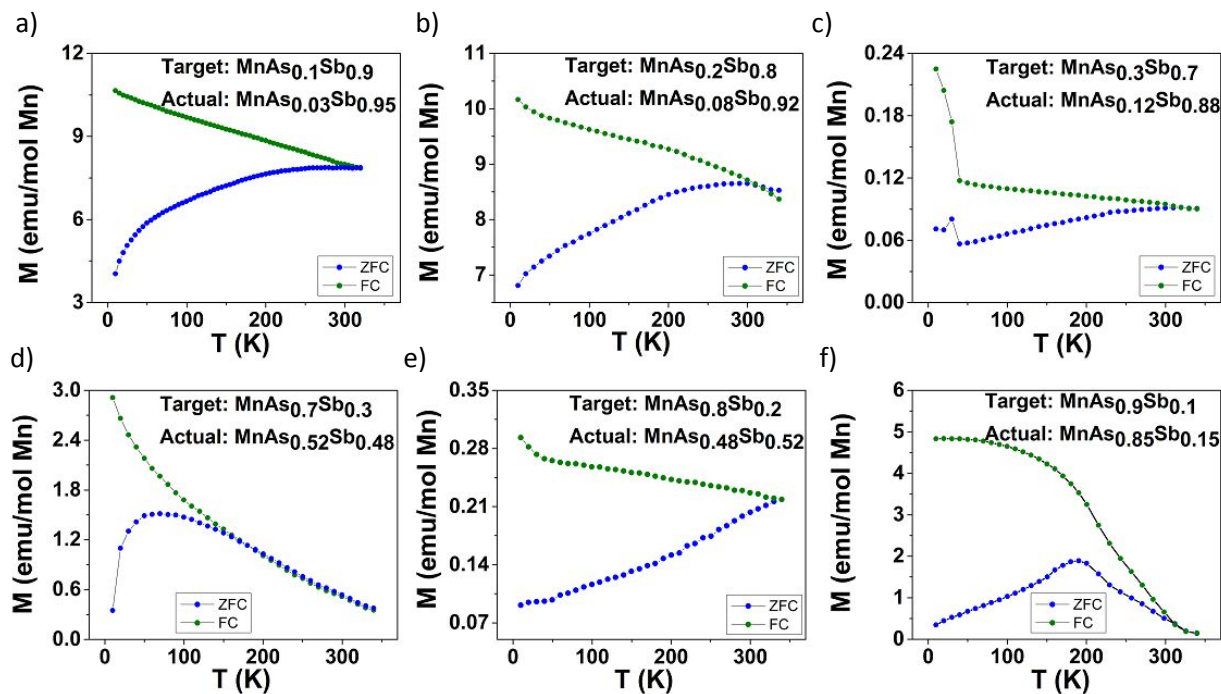
Fig. 10: Temperature dependence of the DC molar magnetization (*M*) (normalized to Mn moles) recorded under Zero-Field-Cooled (ZFC) and Field-Cooled (FC) conditions (collected at 100 Oe) for the actual nanoparticle composition of **(a)** $MnAs_{0.03}Sb_{0.95}$, **(b)** $MnAs_{0.08}Sb_{0.92}$, **(c)** $MnAs_{0.12}Sb_{0.88}$, **(d)** $MnAs_{0.52}Sb_{0.48}$, **(e)** $MnAs_{0.48}Sb_{0.52}$, and **(f)** $MnAs_{0.85}Sb_{0.15}$. The inset shows an enlarged image of the loop of the hysteresis curves obtained at 300 K and 50 K.

According to **Fig. 9a,** The FC plot of $MnAs_{0.31}Sb_{0.69}$ shows a monotonous increase of molar magnetization with a decrease of temperature from 320 K, suggestive of a Curie temperature well in excess of 320 K, as would be expected for a bulk phase of similar composition (ca 380 K) or a more Sb-rich phase, as implicated by the lattice parameters.[45] In the corresponding ZFC curve, the sample is largely temperature independent, intersecting the FC curve at the highest measured temperature (ca 320 K). As shown in **Fig. 9b**, the sample retains significant coercivity at 300 K relative to 50 K (200 Oe vs. 500 Oe). Together, these data suggest T_B is $\geq$ 320 K.
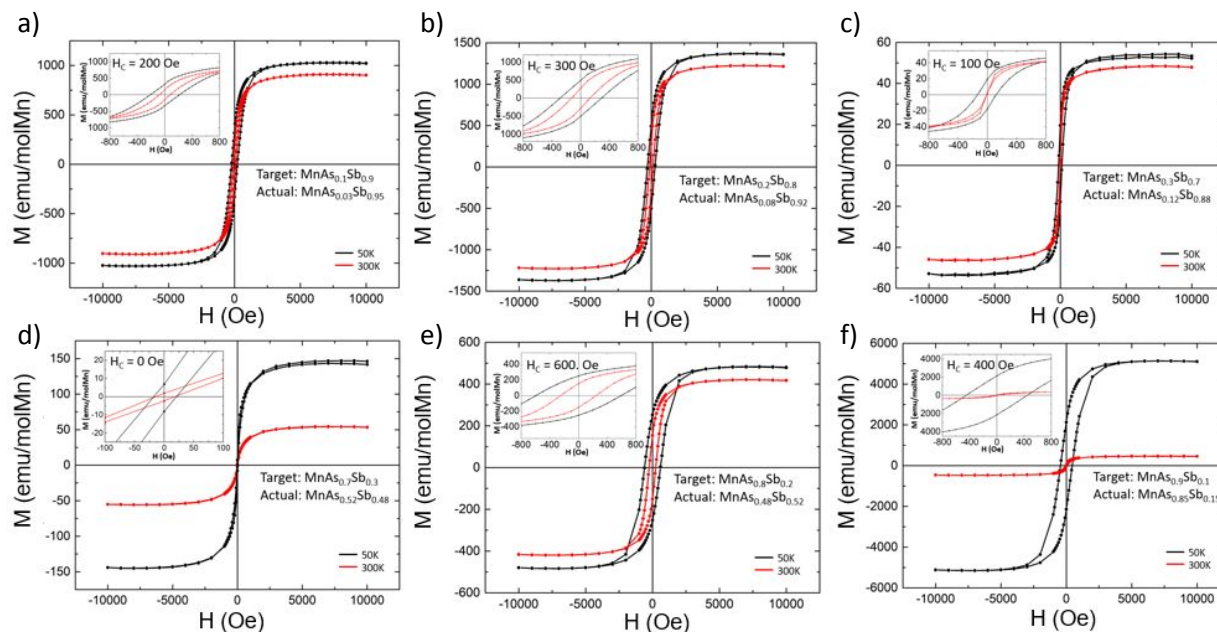
Fig. 11: Field dependence of the DC molar magnetization (M) (normalized to Mn moles) recorded at different magnetic fields (H) at 300 K and 50 K for the actual nanoparticle composition of **(a)** $MnAs_{0.03}Sb_{0.95}$, **(b)** $MnAs_{0.08}Sb_{0.92}$, **(c)** $MnAs_{0.12}Sb_{0.88}$, **(d)** $MnAs_{0.52}Sb_{0.48}$, **(e)** $MnAs_{0.48}Sb_{0.52}$, and **(f)** $MnAs_{0.85}Sb_{0.15}$. The inset shows an enlarged image of the loop of the hysteresis curves obtained at 300 K and 50 K.

As shown in **Fig. 10 a,b,e** and **Fig. 11 a,b,e**, $MnAs_{0.03}Sb_{0.95}$, $MnAs_{0.08}Sb_{0.92}$, and $MnAs_{0.48}Sb_{0.52}$ are qualitatively similar to $MnAs_{0.31}Sb_{0.69}$. In the M vs T plot, there is no definitive maximum in the ZFC to the highest measured temperature (320 K) and the FC curve increases linearly with decreasing temperature ($T_C \gg$ 320 K). Likewise, the M vs. H plots are characterized by a significant room temperature (300 K) hysteresis, all of which suggests the superparamagnetic transition is above 320 K. In contrast, $MnAs_{0.12}Sb_{0.88}$, $MnAs_{0.52}Sb_{0.48}$, and $MnAs_{0.85}Sb_{0.15}$ exhibit a peak in the ZFC at ca 50 K, 300 K, and 200 K, respectively, and while the FC plots do not vary linearly with temperature (**Fig. 10 c,d,f**), nor do they exhibit definitive evidence of the Curie transition except for $MnAs_{0.85}Sb_{0.15}$, which exhibits an upturn in the FC plot upon cooling just below 320 K (T_C is expected to be ca 315 K for this phase vs > 320 K for $MnAs_{0.12}Sb_{0.88}$ and $MnAs_{0.52}Sb_{0.48}$). Additionally, the *M* vs. *H* plots show no coercivity at 300 K (or, for the case of

21

MnAs$_{0.52}$Sb$_{0.48}$, at 50 K), as shown in **Fig. 11 c,d,f**, consistent with superparamagnetism. In this context, the peaks in the ZFC are presumed to correlate with the blocking temperature, T_B.

In order to better understand the magnetic characteristics of these different materials, we sought to build up a relationship between the magnetic data obtained for the bulk compositions of MnAs$_{0.03}$Sb$_{0.95}$, MnAs$_{0.08}$Sb$_{0.92}$, MnAs$_{0.12}$Sb$_{0.88}$, MnAs$_{0.31}$Sb$_{0.69}$, MnAs$_{0.48}$Sb$_{0.52}$, MnAs$_{0.52}$Sb$_{0.48}$, and MnAs$_{0.85}$Sb$_{0.15}$ with the compositional inhomogeneity we know to be present from elemental mapping. Note that the reported saturation magnetization moment for bulk compositions of MnAs$_x$Sb$_{1-x}$ over all x changes only in the short range of 3.4-3.6 μ_B/mol Mn.[58, 59] Accordingly, the saturation magnetization at 50 K for the ferromagnetic MnAs$_x$Sb$_{1-x}$ nanoparticles was determined (after subtracting the paramagnetic background, see **Table S1, ESI†**) and are shown in **Table 3**. The measured magnetic moment for all compositions was considerably smaller than that which should have resulted from ferromagnetic nanoparticles of a given size with the magnetic moment of ~3.5 μ_B per Mn. Based on the results of these measurements and the saturation magnetization taken to be 3.5 μ_B /mol Mn, we calculated the sizes of the respective spherical particles required to produce the corresponding moments. The sizes of the particles determined in this procedure were compared to the normalized data of the experimental particle sizes determined from TEM (see **Table 3**), where r/R is the ratio of the core radius r to the entire nanoparticle radius R. The computed normalized radius for MnAs$_{0.31}$Sb$_{0.69}$ ($r/R = 0.35$) is in good agreement with the results of elemental line scan data, with $r/R \sim 1/3 = 0.33$ (see **Fig. 7**). Note that an alternative explanation (that it is the shell and not the core that is magnetic) can be excluded, because the corresponding normalized radius r/R in this case would be much larger ~ 0.8 (due to the cubic size dependence of the volume). This assumption cannot be reconciled with the TEM results, even assuming that the magnetic data reflects the size averaged over the entire ensemble of the nanoparticles, while

the TEM results represent just a few randomly selected nanoparticles. Our conclusion is also consistent with the results of elemental scans and the fact that the core is crystalline, whereas the shell is amorphous.

The relationship between coercivity and the nanoparticle core size for single domain nanoparticles of the same composition and crystal structure should satisfy the equation $1 - H_c/H_{c0}$ $= AD^{-3/2}$, where H_c is the intrinsic nanoparticle coercivity, H_{c0} is the limiting (maximum) coercivity value for the largest single domain nanoparticle (approximated to be the maximum coercivity measured, 600 Oe), D is the nanoparticle (core) size, and A is a constant related to the upper particle size limit for superparamagnetic behavior.[60] We were surprised to find that, despite the compositional and size variation, a linear fit of the plot $1 - H_c/H_{c0}$ as a function of the core size D in semi-log scale (**Fig. 12**) delivers a slope of $t = -1.49$, very close to the theoretical value for single-domain particles, $t = -3/2$. This implies that in this system the magnetic anisotropy (which generally affects the magnitude of the coercivity) does not change systematically with the particle composition and size. Nevertheless, significant point-by-point variation is observed in the plot (note, for example, the highly coercive 3 nm particles), pointing to polydispersity in composition and size. More detailed magnetic measurements with monodisperse nanoparticles are necessary to confirm these preliminary observations.

In considering the data in **Fig. 12**, it should be noted that $1 - H_c/H_{c0}$ goes to zero when $H_c = H_{C0}$, which corresponds to the maximum particle size for a single domain particle (D_s, ~7 nm based on the fitted line). These data imply that the synthesized $MnAs_{0.85}Sb_{0.15}$ sample (red circle) may be multi-domain, since it is less coercive than would be predicted based on its size.

However, we note that the deviation from the fit may instead reflect a different degree of magnetocrystalline anisotropy relative to the other phases, possibly associated with the fact that this phase is unique among all others studied here in that it undergoes a first-order phase transition to the MnP-type structure.

Of the phases adopting the NiAs-type structure at room temperature, the largest ferromagnetic Mn portion is in the $MnAs_{0.31}Sb_{0.69}$ composition, which has the highest saturation magnetization and the largest core size. In contrast, the low moment evident in the $MnAs_{0.12}Sb_{0.88}$ composition is reflective of a very small core. We caution that the extent of phase-segregation is likely to depend sensitively on synthetic parameters, and not necessarily on the target or actual composition. As is evident in **Table 3**, the actual compositions for targets x = 0.7 and x = 0.8 are quite similar (x = 0.52 and x = 0.48, respectively), but the former is characterized by zero coercivity and a very small saturation magnetization whereas the latter has the greatest coercivity of all measured samples and a saturation magnetization 5x greater than the former.

Table 3: Composition-dependent magnetic properties at 50 K, experimentally determined particle sizes R (diameter) from electron microscopy measurements, ratio of core to overall particle diameter (r/R) used to compute core size (diameter) based on M_s (see **Figs. 3, 4**).

Target Composition	Actual Composition	Saturation Magnetization (M_s), 50 K (μ_B/mol Mn)	Coercivity, 50K (Oe)	TEM Diameter, R (nm)	r/R Computed from M_s	Core Diameter, r (nm)
$MnAs_{0.1}Sb_{0.9}$	$MnAs_{0.03}Sb_{0.95}$	0.100623 (38)	200. ± 15	10.9 ± 0.89	0.31	3.36 ± 0.27
$MnAs_{0.2}Sb_{0.8}$	$MnAs_{0.08}Sb_{0.92}$	0.110215 (45)	300. ± 15	10.9 ± 1.3	0.32	3.48 ± 0.41
$MnAs_{0.3}Sb_{0.7}$	$MnAs_{0.12}Sb_{0.88}$	0.0057846 (81)	100. ± 25	11.9 ± 2.0	0.12	1.44 ± 0.24
$MnAs_{0.5}Sb_{0.5}$	$MnAs_{0.31}Sb_{0.69}$	0.146687 (29)	500. ± 5.0	13.0 ± 1.5	0.35	4.56 ± 0.53
$MnAs_{0.7}Sb_{0.3}$	$MnAs_{0.52}Sb_{0.48}$	0.00986148 (41)	0 ± 20.	11.4 ± 2.0	0.14	1.63 ± 0.29
$MnAs_{0.8}Sb_{0.2}$	$MnAs_{0.48}Sb_{0.52}$	0.0548859 (7.0)	600. ± 8.0	12.0 ± 1.3	0.26	3.05 ± 0.33
$MnAs_{0.9}Sb_{0.1}$	$MnAs_{0.85}Sb_{0.15}$	0.442952 (41)	400. ± 20.	13.4 ± 1.3	0.51	6.78 ± 0.66

It is also worth noting that the two apparently "smallest" core sizes (with the smallest reduced coercivities) are also characterized by a T_B <300 K, in contrast to all of the other samples

adopting the NiAs-type. This is evident in the M vs. H plots (**Fig. 11 c, d**) as an absence of magnetic

hysteresis for the 300 K plot and in the M vs. T plots by a maximum in the ZFC at ca 300 K for

$MnAs_{0.12}Sb_{0.88}$ (**Fig. 10c**) and at ca 75 K for $MnAs_{0.52}Sb_{0.48}$ (**Fig. 10d**). This is expected, as

particles of the critical size have zero coercivity at their blocking temperature, and thus for uniaxial

particles, $H_c/H_{c0} = 1 - \left(T/T_B\right)^{\frac{1}{2}}$. The one sample adopting the orthorhombic MnP-type structure

at room temperature (target x = 0.1, observed x = 0.15) is also superparamagnetic at room

temperature (**Fig. 11 f**) with a T_B of ca 200 K (**Fig. 10f**), but this is not surprising since bulk samples

of MnAs doped with up to 10% Sb have composition independent T_C's of ca 315 K (recall that T_C

represents the upper temperature limit for T_B). Based on the targeted compositions, we would have

expected to realize samples with T_C's as low as 240 K (x = 0.7) for samples adopting the NiAs-

type, but the observed composition limits x to 0.5, for a minimum T_C of ~340 K. If in fact the

magnetic properties correspond to the crystalline phase indicated by the lattice parameters, x is

limited to 0.2, corresponding to a minimum T_C of 480 K. Either of these scenarios are consistent

with our observations.
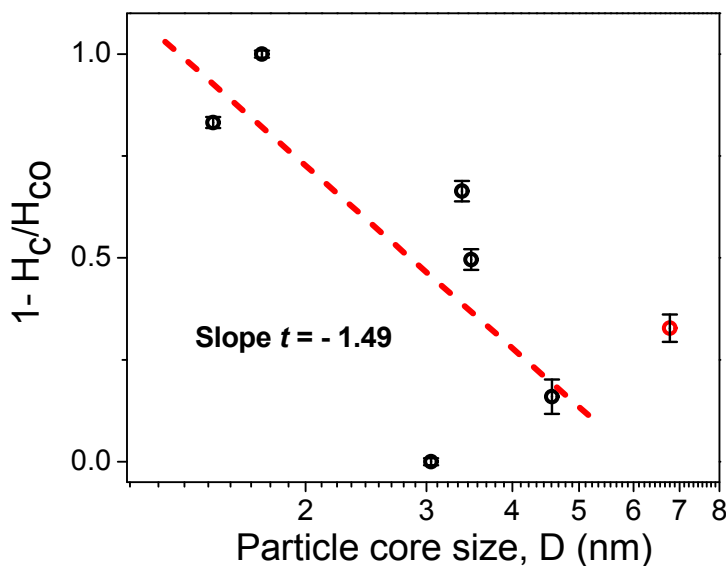
Fig. 12: The relationship between the reduced coercivity at 50 K and the core diameter D for $MnAs_xSb_{1-x}$ adopting the NiAs structure type at 50 K. The red circle corresponds to $MnAs_{0.85}Sb_{0.15,}$ which is not included in the fit as it is unique among all of the phases in undergoing a first order phase transition to the MnP-type near room-temperature.

Conclusions

Colloidal synthesis of $MnAs_xSb_{1-x}$ (x = 0.1 - 0.9) nanoparticles results in phase segregation rather than the expected solid-solution formation obtained under a strong thermodynamic driving force (i.e., high temperature). The crystalline core comprises Mn, As and Sb, whereas the amorphous shell consists of $MnSb_aO_b$ where a = 0 or 1. Compositional analysis of the ensemble indicates that As incorporation is limited relative to Sb incorporation in the composition space where only the NiAs structure-type is adopted ($0 \leq x \leq 0.85$); maximum As incorporation corresponds to x = ~0.5. However, an analysis of lattice parameters suggests that the As incorporation in the crystalline $MnAs_xSb_{1-x}$ core may actually be limited to as little as x = ~0.2 suggesting a formulation $MnAs_{0.2-y}Sb_{0.8+y}$ for experimentally realized phases where $x \leq 0.85$.

Despite the inhomogeneity, a simple magnetic model based on the fact that the ferromagnetic moment is (in reference to bulk phases) largely unchanged as a function of composition allows us to conclude that the crystalline core is ferromagnetic, while the amorphous shell is paramagnetic. Notably, the relationship between the inferred crystallite size and the observed coercivity at 50 K follows the expected trend for single domain particles. While phase inhomogeneities *per se* may not significantly limit the magnetocaloric behavior, and may in fact broaden the temperature range over which a significant response can be attained, the extensive oxide component is more problematic as it represents a large fraction of the material volume that does not contribute to generation of magnetic entropy. Current work is focused on optimizing the synthesis to achieve reproducible and predictable core sizes/compositions and limit surface oxide via elimination of oxygen-containing reagents (trioctylphosphine oxide, triphenylarsine oxide) and/or post-synthetic reduction strategies.

References

1. A. Dutta and N. Pradhan, *J. Phys. Chem. Lett.*, 2017, **8**, 144-152.
2. S. Carenco, D. Portehault, C. Boissière, N. Mézailles and C. Sanchez, *Adv. Mater.*, 2014, **26**, 371-390.
3. S. Carenco, D. Portehault, C. Boissière, N. Mézailles and C. Sanchez, *Chem. Rev.*, 2013, **113**, 7981-8065.
4. S. Mourdikoudis and Z. Sofer, *CrystEngComm*, 2021, *Advance Article*, DOI: 10.1039/D0CE01766C.

5.   D. G. Ramlan, S. J. May, J.-G. Zheng, J. E. Allen, B. W. Wessels and L. J. Lauhon, *Nano Lett.*, 2006, **6**, 50-54.

6.   K. H. Ploog, *Physica E: Low-dimensional Systems and Nanostructures*, 2004, **24**, 101-106.

7.   T. Hanna, D. Yoshida and H. Munekata, *J. Cryst. Growth*, 2011, **323**, 383-386.

8.   R. P. Madhogaria, C.-M. Hung, B. Muchharla, A. T. Duong, R. Das, P. T. Huy, S. Cho, S. Witanachchi, H. Srikanth and M.-H. Phan, *Phys. Rev. B*, 2021, **103**, 184423.

9.   J. A. Cooley, M. K. Horton, E. E. Levin, S. H. Lapidus, K. A. Persson and R. Seshadri, *Chem. Mater.*, 2020, **32**, 1243-1249.

10.   V. Franco, J. S. Blázquez, J. J. Ipus, J. Y. Law, L. M. Moreno-Ramírez and A. Conde, *Prog. Mater. Sci.*, 2018, **93**, 112-232.

11.   M. F. J. Boeije, P. Roy, F. Guillou, H. Yibole, X. F. Miao, L. Caron, D. Banerjee, N. H. van Dijk, R. A. de Groot and E. Brück, *Chem. Mater.*, 2016, **28**, 4901-4905.

12.   V. Franco, J. S. Blázquez, B. Ingale and A. Conde, *Annu. Rev. Mater. Res.*, 2012, **42**, 305-342.

13.   L. Tocado, E. Palacios and R. Burriel, *J. Appl. Phys.* , 2009, **105**, 093918-093913.

14.   Y. Takagaki, B. Jenichen, C. Herrmann, E. Wiebicke, L. Däweritz and K. H. Ploog, *Phys. Rev. B*, 2006, **73**, 125324.

15.   Y. Takagaki, C. Herrmann, E. Wiebicke, J. Herfort, L. Däweritz and K. H. Ploog, *Appl. Phys. Lett.*, 2006, **88**, 032504.

16.   Y. Takagaki, J. Herfort, L. Däweritz and K. H. Ploog, *Phys. Rev. B*, 2006, **74**, 224417.

17.   R. Engel-Herbert, T. Hesjedal, J. Mohanty, D. M. Schaadt and K. H. Ploog, *Phys. Rev. B*, 2006, **73**, 104441.

18.   J. Mira, F. Rivadulla, J. Rivas, A. Fondado, T. Guidi, R. Caciuffo, F. Carsughi, P. G. Radaelli and J. B. Goodenough, *Phys. Rev. Lett.*, 2003, **90**, 097203.

19.   J. B. Goodenough and J. A. Kafalas, *Phys. Rev.*, 1967, **157**, 389-395.

20.   V. I. Mitsiuk, G. A. Govor and M. Budzyński, *Inorg Mater*, 2013, **49**, 14-17.

21.   N. K. Sun, F. Liu, Y. B. Gao, Z. Q. Cai, B. S. Du, S. N. Xu and P. Z. Si, *Appl. Phys. Lett.*, 2012, **100**, 112407.

22.   N. Sun, S. Xu, D. Li and Z. Zhang, *Phys. Stat. Solidi A*, 2011, **208**, 1950-1952.

23.   H. Fjellvag, A. F. Andresen and K. Bärner, *J. Magn. Magn. Mater.*, 1984, **46**, 29-39.

24.   A. Roger and R. Fruchart, *Mat. Res. Bull.*, 1968, **3**, 253-264.

25.   R. Caballero-Flores, V. Franco, A. Conde, L. F. Kiss, L. Peter and I. Bakonyi, *J. Nanosci. Nanotechnol.*, 2012, **12**, 7432-7436.

26.   P. Govindappa, P. V. Trevizoli, I. Niknia, T. V. Christiaanse, R. Teyber and A. Rowe, *J. Appl. Phys.*, 2018, **124**, 134901.

27.   M. R. Dudek, K. K. Dudek, W. Wolak, K. W. Wojciechowski and J. N. Grima, *Sci. Rep.*, 2019, **9**, 17607.

28.   V. Chaudhary and R. V. Ramanujan, *Sci. Rep.*, 2016, **6**, 35156.

29.   S. K. Vandrangi, J.-C. Yang, Y.-M. Zhu, Y.-Y. Chin, H.-J. Lin, C.-T. Chen, Q. Zhan, Q. He, Y.-C. Chen and Y.-H. Chu, *ACS Appl. Mater. Interface*, 2015, **7**, 26504-26511.

30.   P. Lampen, N. S. Bingham, M. H. Phan, H. Kim, M. Osofsky, A. Piqué, T. L. Phan, S. C. Yu and H. Srikanth, *Appl. Phys. Lett.*, 2013, **102**, 062414.

31.   V. K. Pecharsky, J. Cui and D. D. Johnson, *Philos. Trans. R. Soc., A.*, 2016, **374**, 20150305.

32.   J. D. Moore, K. Morrison, G. K. Perkins, D. L. Schlagel, T. A. Lograsso, K. A.
        Gschneidner, V. K. Pecharsky and L. F. Cohen, *Adv. Mater.*, 2009, **21**, 3780-3783.
33.   K. Senevirathne, R. Tackett, P. R. Kharel, G. Lawes, K. Somaskandan and S. L. Brock,
        ACS Nano, 2009, **3**, 1129-1138.
34.   Y. Zhang, R. Regmi, Y. Liu, G. Lawes and S. L. Brock, *ACS Nano*, 2014, **8**, 6814-6821.
35.   M. A. Hettiarachchi, E. Abdelhamid, B. Nadgorny and S. L. Brock, *J. Mater. Chem. C*,
        2016, **4**, 6790-6797.
36.   R. Pimmachcharige, Y. Zhang, R. Regmi, G. Lawes and S. L. Brock, *J. Mater. Chem. C,*
        2017, **5**, 3352-3358.
37.   M. A. Hettiarachchi, E. Abdelhamid, B. Nadgorny and S. L. Brock, *Nanoscale*, 2019, **11**,
        6886-6896.
38.   A. T. Sathyanarayana and A. Mani, *J. Alloys Compd.*, 2021, **862**, 158322.
39.   A. de Campos, M. S. da Luz, A. de Campos, A. A. Coelho, L. P. Cardoso, A. O. dos
        Santos and S. Gama, *J. Magn. Magn. Mater.*, 2015, **374**, 342-344.
40.   A. Dahani, S. Kacimi, A. Boukortt, M. Bououdina and A. Zaoui, *J. Supercon. New
        Magn.*, 2014, **27**, 2263-2275.
41.   L. G. de Medeiros, N. A. de Oliveira and A. Troper, *J. Alloys Compd.* 2010, **501**, 177-
        182.
42.   H. Wada, C. Funaba and T. Asano, *Mater. Trans.*, 2006, **47**, 486-491.
43.   H. Wada, K. Taniguchi and Y. Tanabe, *Mater. Trans.*, 2002, **43**, 73-77.
44.   H. Wada and Y. Tanabe, *Appl. Phys. Lett.*, 2001, **79**, 3302-3304.
45.   L. R. Edwards and L. C. Bartel, *Phys. Rev. B*, 1972, **5**, 1064-1072.
46.   N. Sirota and E. Vasilev, *Phys. Stat. Sol. (b)*, 1968, **28**, K175-K177.
47.   Y. Wang, J. He, C. Liu, W. H. Chong and H. Chen, *Angew. Chem. Int. Ed.,* 2015, **54**,
        2022-2051.
48.   C. Burda, X. Chen, R. Narayanan and M. A. El-Sayed, *Chem. Rev.*, 2005, **105**, 1025-
        1102.
49.   A. Zorko, O. Adamopoulos, M. Komelj, D. Arčon and A. Lappas, *Nat. Commun.*, 2014,
        5, 3222.
50.   S. Carenco, X. F. Le Goff, J. Shi, L. Roiban, O. Ersen, C. Boissière, C. Sanchez and N.
        Mézailles, *Chem. Mater.*, 2011, **23**, 2270-2277.
51.   H. Zhang, J. Ding, G. Chow, M. Ran and J. Yi, *Chem. Mater.*, 2009, **21**, 5222-5228.
52.   Y. Zhang, N. Li, Z. Zhang, S. Li, M. Cui, L. Ma, H. Zhou, D. Su and S. Zhang, *J. Am.
        Chem. Soc.*, 2020, **142**, 8490-8497.
53.   C. Wang, H. Daimon and S. Sun, *Nano Lett.*, 2009, **9**, 1493-1496.
54.   F. Wang, R. Tang, J. L.-F. Kao, S. D. Dingman and W. E. Buhro, *J. Am. Chem. Soc.*,
        2009, **131**, 4983-4994.
55.   G. Kieslich, C. S. Birkel, A. Stewart, U. Kolb and W. Tremel, *Inorg. Chem.*, 2011, **50**,
        6938-6943.
56.   L. Kumari, W. Li, J. Y. Huang and P. P. Provencio, *J. Phys. Chem. C*, 2010, **114**, 9573-
        9579.
57.   K. Motizuki, H. Ido, T. Itoh and M. Morifuji, 2010.
58.   B. K., *Phys. Stat. Sol. (b)*, 1977, **84**, 385-392.
59.   K. Barner, *Phys. Stat. Sol. (a)*, 1971, **5**, 405-413.
60.   E. F. Kneller and F. E. Luborsky, *J. Appl. Phys.*, 1963, **34**, 656-658.